

# RESIST: Remapping EIT Signals Using Implicit Spatially-Aware Transformer

**Dominik Becker**

*Institute of Computer Science and Campus Institute Data Science, University Göttingen, Germany*

**Anita Just,**

**Günter Hahn,**

**Peter Herrmann,**

**Leif Saager,**

*University Medical Center Göttingen, Germany*

**Fabian Sinz**

*Institute of Computer Science and Campus Institute Data Science, University Göttingen, Germany*

DOMINIK.BECKER@INFORMATIK.UNI-GOETTINGEN.DE

ANITA.JUST@MED.UNI-GOETTINGEN.DE

GHAHN@GWDG.DE

PHERRMANN@MED.UNI-GOETTINGEN.DE

LEIF.SAAGER@MED.UNI-GOETTINGEN.DE

SINZ@UNI-GOETTINGEN.DE

## Abstract

Electrical impedance tomography (EIT) aims to reconstruct the body’s internal electrical conductivity distribution from surface voltage measurements. This non-invasive, non-ionizing, and cost-effective technique is valuable for medical applications, offering potential for long-term monitoring of lung functionality and condition. However, existing methods of absolute EIT provide blurred tomograms that are difficult to interpret, do not resemble the human topography and are therefore of limited use for clinical applications. We propose RESIST, a new data-driven approach that integrates prior geometry of human bodies and conductivity information by combining an implicit neural network with a transformer model in an encoder-decoder framework. RESIST maps simultaneous EIT measurements from multiple body levels to conductivity values at any coordinate in a 3D body volume. We train RESIST on simulated EIT measurements based on 3D human body CT segmentations. We find that it is robust against distortions in the signal and exact placement of electrodes, correctly infers interpolation laws, and generalizes to real EIT measurements in humans.

**Keywords:** EIT, Transformer, Implicit Networks

**Data and Code Availability** We use anonymized CT images from The Cancer Imaging Archive (TCIA) ([Gatidis and Kuestner, 2022](#)). The use of the data set was granted by a restricted licence agreement with the TCIA. The code can be accessed via this [link](#).

**Institutional Review Board (IRB)** The study was approved on 02.01.2023 by the Institutional Review Board (IRB) of the University Medical Center Göttingen and registered with the German Clinical Trial Registry [DRKS00033243](#).

## 1. Introduction

Obtaining information about internal properties of a body is a difficult and mostly ill-posed inverse problem. Most methods record signals outside the body that have been influenced by internal properties of the body. Inverting these measurements to obtain the internal structure underlying the observations is at the heart of all those methods.

In this work, we focus on electrical impedance tomography (EIT), which aims to reconstruct the electrical conductivity or resistivity distribution of the body by measuring potential differences of electrical signals on the surface. To this end, electrodes are attached on the skin and current is fed into the body via electrode pairs while all other electrode pairs record potential differences. These measurements are used to create a tomogram that reflects the conductivity distribution within the body. The method is particularly interesting for medical applications as it is non-invasive, non-ionizing, inexpensive and does not require large machinery. It therefore offers the potential of long-term recordings for patients at the bedside. One prime target for these recordings are lungs. Unlike most tissue in the body, the conductivity of the lungs changes considerably during a breathing cy-

cle. Moreover, the contrast in conductivity between lung tissue and other internal tissue types, like the heart, vessels or bones, is comparably high, enabling clear distinction in conductivity tomograms.

EIT is already used in clinical practice, primarily using functional EIT (f-EIT, Frerichs et al., 2017) which compares EIT sequences over time and applies a backprojection algorithm (e.g., Adler et al., 2009) to generate a tomogram. However, f-EIT is limited by its reliance on reference measurements, making it difficult to detect abnormalities or monitor long-term changes.

Absolute EIT (a-EIT), which reconstructs conductivity from a single time point without a reference, is a highly ill-posed problem and typically requires prior information or regularization (e.g., Hamilton et al., 2016; Liu et al., 2018). Those priors must be constructed by external knowledge about the properties of the domain, e.g. the shape of the lungs or the body of a patient. However, obtaining this information can be challenging and could even require a CT or MRI. To avoid this step, we integrate prior information about body shape via a data-driven approach.

In recent years, there have been substantial developments in data-driven prior inclusion with deep learning methods, such as variational autoencoder (Kingma and Welling, 2022), score/diffusion models (Ho et al., 2020; Song et al., 2021), and non-probabilistic, learnable priors, such as implicit neural networks (Mescheder et al., 2019; Sitzmann et al., 2020; Mildenhall et al., 2021). In computer vision, implicit neural networks can learn a smooth function over input coordinates which can be conditioned on domain-specific features (Peng et al., 2020; Yu et al., 2021). While implicit networks can be used to learn a spatial prior over coordinates of an output space, transformer models (Vaswani et al., 2017) have been proven an effective backbone architecture in processing different kinds of unstructured data in a vast number of domains (e.g., Radford et al., 2018; Dosovitskiy et al., 2020; Jumper et al., 2021).

Here, we propose a model for remapping EIT signals using an implicit spatially-aware transformer (RESIST). RESIST follows an encoder-decoder framework that simultaneously maps EIT measurements from multiple body levels to conductivity values at any coordinate in a 3D body volume. At first, EIT electrode measurements are encoded into a latent space using a transformer. From this, conductivity signals are decoded using an implicit network that outputs the conductivity at a queried spatial position

in the volume given the latent state. The coordinate-based query of conductivity values in the body volume allows for an implicit inclusion of prior geometry and conductivity information of the human body. In addition, the transformer-based encoding of EIT signals provides a powerful and flexible extraction of important features from EIT measurements that can vary in length or the number of applied electrodes (see backward model in Figure 1).

Training the network requires pairs of EIT measurements and conductivity volumes. Since those are generally not observable in the living human patient, we simulate absolute EIT measurements using finite element methods (FEM) and train RESIST to invert the mapping from conductivity volume to electrode measurements. To this end, we use a data set containing CT images of 266 subjects. We segment the CT images, generate a volume mesh and simulate the EIT measurements with pre-defined tissue-specific conductivity values (see forward model in Figure 1).

We show that RESIST is able to reconstruct the lung conductivity in easily interpretable tomograms for both simulated and real EIT measurements. Moreover, these tomograms reflect human topography, while being robust to noise on signals and electrode positions.

## 2. Related Work

Previous approaches for solving the inverse problem of EIT can be grouped into three broad categories: model based, learning based, and mixed forms. The model based D-Bar method (Siltanen et al., 2000; Mueller and Siltanen, 2003; Knudsen et al., 2007; Hamilton et al., 2020) is a direct numerical solution of the EIT problem utilizing the Dirichlet-to-Neumann map. In principle, D-Bar makes it possible to define a prior over different geometries (Alsaker and Mueller, 2016; Alsaker et al., 2017; Alsaker and Mueller, 2018; Hamilton et al., 2016). However, the prior must be estimated or explicitly defined, which requires the recording and segmentation of a CT/MRI when used in a clinical context. Hamilton et al. (2020) also extended the 2.5D D-Bar method to a spherical 3D space. Another example is the SIRT algorithm. SIRT (Just et al., 1998, 2007), is an iterative algorithm that constructs beams for apparent resistivities over a 2D grid of cells. The apparent resistivities are derived from the measured potential differences, current and a shape-related geometric factor. In each iteration a

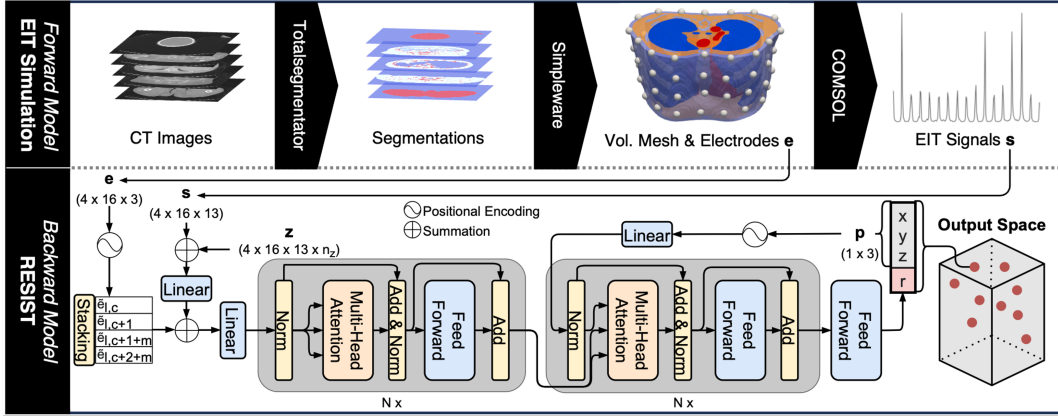


Figure 1: The forward model enables the FEM simulation of EIT signals using volume meshes created from CT segmentations and pre-defined electrode positions. For real life application, these signals are replaced by the EIT measurement on the patient. RESIST takes signals  $s$ , electrode positions  $e$  and coordinates from the output space  $p$  and predicts the conductivity  $r$  for the given coordinates.

weighting matrix changes the predicted resistivity in the grid cells dependent on the difference in the apparent resistivities from measurements and the forward model from the previous iteration until convergence. This approach was applied with modifications in Hahn et al. (2006) and Hahn et al. (2013).

Adler and Guardo (1994) were the first to use neural networks to generate images of conductivity change, similar to f-EIT, for a simplified triangle mesh in 2D. Various different approaches have been applied since, using non-linear fully connected networks (Wang et al., 2009; Li et al., 2019) or convolutional networks (Fan and Ying, 2020; Wu et al., 2021). Other recent learning based methods operate in 3D space to detect objects with different conductivity (Chen et al., 2020; Ye et al., 2023) or use a linear reconstruction with regularization on a small grid of voxels for cell imaging (Yang et al., 2017).

Examples for mixed forms are Deep D-Bar (Hamilton and Hauptmann, 2018) and point cloud transformer (Yoo et al., 2023). Deep D-Bar uses the direct D-Bar reconstruction algorithm to get an initial 2D tomogram and subsequently a 2D convolutional Unet to postprocess the initial tomogram. The point cloud transformer operates in 3D by first mapping the EIT signals and electrode positions to a latent space using a transformer encoder. Then a conventional reconstruction algorithm is used to get a first guess for the 3D location of point clouds belonging to high or

low conductive objects. Eventually, the latents and the point clouds are processed by a transformer decoder to find a more precise 3D point cloud of those objects.

All EIT reconstruction methods above use simple examples to simulate the EIT measurements. This involves either real measurements using a phantom and simple geometries with different values (e.g., Alsaker and Mueller, 2018; Yoo et al., 2023) or segmenting 2D masks of lung and body shape from real CT images and expanding those 2D representations along a third dimension to obtain a volume (2.5D) (e.g., Just et al., 2007; Wu et al., 2021).

However, in real humans are strong differences in the conductivity of bones, fat or muscles surrounding the lungs, with the proportions of these tissues varying greatly between individuals. Furthermore, electrical current flows in 3D space and not in 2D slices. Therefore, variations in conductivity along the vertical axis should be accounted for.

In order to get closer to the complexity of the true conductivity distribution of human bodies, we do not use EIT measurements from phantom experiments or simulations with 2.5D volumes, but use 3D segmentations of CT images to generate 3D models of human bodies for our simulations. The simulation of EIT signals on topographically correct 3D models of human bodies offers a significant step towards realistic data generation compared to previous methods. Data

pairs of spatial conductivity distribution and EIT signals enable the development of models that allow a stronger data-driven incorporation of spatial prior information that is necessary because of the ill-defined nature of EIT reconstruction. Unlike other reconstruction algorithms, the RESIST model exploits the topographic information in the data without manually defining a prior and provides interpretable tomograms that match human topography. RESIST thus opens the way for a-EIT reconstruction of conductivity distributions in more complex geometries than phantoms or 2.5D volumes.

Due to its implicit properties, RESIST generates tomograms by flexibly slicing through a smooth and continuous 3D space (Appendix B.3) while most a-EIT reconstruction algorithms, like SIRT or Deep D-Bar, generate only 2D tomograms. Yoo et al. (2023) and Ye et al. (2023) return a 3D output, but either generate a pointcloud of the surface or detect sparse voxels of objects. Those methods are not suited for lung monitoring since we are primarily interested in the dense conductivity distribution within lungs and not in their shape. Other 3D methods (Hamilton et al., 2020; Fan and Ying, 2020) cannot be easily generalized to complex shapes like human bodies.

RESIST uses a transformer encoder and decoder to process EIT signals and spatial information. The combination of transformer and implicit networks has already been used in the domain of super resolution. Cao et al. (2023) uses cross-attention to integrate local features into a continuous 2D space of images. Chen and Wang (2022), on the other hand, uses a meta-learning approach to directly learn the weights of an implicit network via a transformer model. RESIST has a similar approach, but does not refer to local features nor does it learn the weights of the implicit network. Instead, the input coordinates are simply conditioned via cross-attention on the encoded global signals.

### 3. Methods

#### 3.1. Forward Model

Training a deep learning model in a supervised fashion requires labeled data. Therefore, we need EIT signals and the true conductivity distribution of the body where these signals originated. In reality, information about the true conductivity distribution can only be approximated from CT or MRI scans by segmenting the individual body tissue types and assign-

ing reasonable conductivity values. Hence, we would need a large data set of patients with both EIT measurements and CT/MRI images to train the model. This would require a costly study and also a high radiation exposure for the test subjects in the case of CT. Instead, we simulate the EIT measurements with FEM by creating volume meshes from segmentation masks of existing CTs. The simulations map from a ground truth (simplified) conductivity distribution to EIT measurements and are therefore called *forward model* (Figure 1).

We use a subset of the FDG-PET-CT-Lesions data set (Gatidis and Kuestner, 2022) from The Cancer Imaging Archive (TCIA) and apply the TotalSegmentator (Wasserthal et al., 2023), a pre-trained 3D nnUNet model (Isensee et al., 2018) for CT image segmentation, to obtain up to 133 individual tissue masks. The segmentation masks were aggregated to reflect five different tissue categories with significant conductivity differences. These are (1) lung tissue, which includes the individual lung lobes and the trachea, (2) heart and blood vessels, (3) bone tissue, (4) fat tissue and (5) background, which includes all other organs and tissue.

After aggregation, we transformed the voxel masks into a volume mesh consisting of 14.8 mio. individual tetrahedra on average. For this, we used the medical imaging tool Simpleware (Synopsys, Inc., 2020). The volume meshes were then imported into COMSOL Multiphysics (Multiphysics, 1998), where each of the tetrahedra retained the tissue label so that a specific conductivity value can be assigned. Subsequently, we placed electrodes in four different levels of the body. The first electrode in each level was placed along a vertical line in  $z$  dimension from the sternum while the others were placed as equidistant from each other as possible, maintaining the middle electrode placed along the vertebral column. Eventually, the FEM solver program Comsol Multiphysics was used to obtain the signals from the volume mesh. A frequency of 50 kHz and an amplitude of 1 mA was used. We applied the Adjacent-Drive method (Garg and Goel, 2013) as EIT measurement scheme. This means, that each measurement cycle has two neighboring feeding electrodes and potential differences are measured at all other neighboring electrode pairs. Figure 2 illustrates the measurement scheme. The green electrodes act as feeding pair, while every other adjacent electrode pair that does not involve one of the feeding electrodes is used as recording electrode pair (electrodes 6 and 7 in Figure 2). With a total of 16 elec-

trodes per level, this results in  $16 \times 13$  potential differences. Taken over four levels, this results in a total of 832 potential differences per entire subject simulation. The conductivity values 0.7, 0.02, 0.025 and 0.3 S/m were assigned to the tissue categories (2), (3), (4) and (5) respectively. The lung tissue was simulated with 0.2, 0.1, 0.07 and 0.05 S/m, whereby a fixed value was used for the entire lung tissue of a subject (Gabriel and Gabriel, 1996; Gabriel et al., 1996). For limitations of this model see Appendix C.

### 3.2. Backward Model

While the forward model simulates the EIT signals using a volume mesh with a fixed conductivity distribution, the backward model has to invert the simulation and reconstruct the underlying conductivity distribution of the signals. In the following we describe the RESIST architecture for the backward model (Figure 1).

**Notation** We use  $s$  for the  $4 \times 16 \times 13$  EIT measurements, where each element  $s_{lcm} \in \mathbb{R}_+$  is the voltage recorded in the  $l$ -th level, with the feeding electrodes  $c$  and  $c+1$  and the recording electrodes  $c+1+m$  and  $c+2+m$ . We refer to a single voltage measurement as *signal* and to all signals obtained with the same feeding electrodes as a *cycle*. For our simulations we use  $l \in [1, 2, 3, 4]$  being the electrode level,  $c \in [1, 2, \dots, 16]$  being the measurement cycle and  $m \in [1, 2, \dots, 13]$  being the signal within one cycle. Figure 2 shows the setting to measure the signal  $s_{1,1,4}$  between electrode 6 and 7 (red) while feeding the current through the electrodes 1 and 2 (green). We denote the coordinate of each electrode as  $e_{lc} \in \mathbb{R}^3$  and the query coordinate as  $p_i \in \mathbb{R}^3$ .

**Embed Spatial Information** We use self-attention blocks to process the EIT signals which enable the exchange of information among the individual measurements. However, using the raw signals without any spatial information leads to the loss of the sequential order of the measurements. In order to keep this information we use the 3D coordinates for the electrodes, which we normalize to  $\mathbb{R}_{[-1,1]}^3$ .

For each signal, four electrodes are required: two electrodes applying the current and two electrodes recording the voltage. Therefore, we first embed the electrode position for all electrodes using a cosine embedding with different fixed frequencies  $f = [1, \dots, n_f]$  (Zhong et al., 2020):

$$\tilde{\mathbf{e}} = [\sin(\pi \cdot 2^{f-2} \cdot e), \cos(\pi \cdot 2^{f-2} \cdot e)]_f^\top,$$

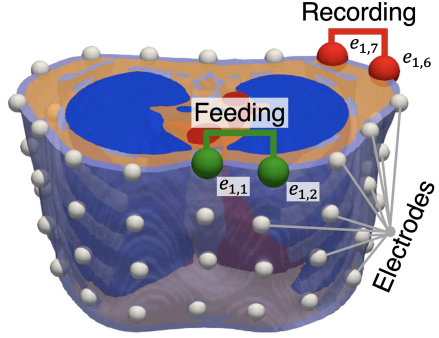


Figure 2: A section of a volume mesh with 64 electrodes over four levels. Feeding electrodes (green) and recording electrodes (red) for the fourth signal of the first measurement cycle in level one are highlighted.

where  $\tilde{\mathbf{e}}$  is of dimensions  $4 \times 16 \times (3 \times 2 \times n_f)$ . For each EIT signal, we stack the positional encoding of the four electrodes involved and obtain positional features that are specific to an individual signal:

$$\tilde{\mathbf{e}}_{l,c,m} = [\tilde{\mathbf{e}}_{l,c}, \tilde{\mathbf{e}}_{l,c+1}, \tilde{\mathbf{e}}_{l,c+1+m}, \tilde{\mathbf{e}}_{l,c+2+m}]^\top.$$

After that, we first add a learned embedding vector  $\mathbf{z}_{l,c,m}$  to the signal and use a linear layer  $g_1$  to match the dimension of the electrode feature. Then, we add electrode and signal features and process them by linear layer  $g_2$ :

$$\tilde{\mathbf{s}}_{l,c,m} = g_2(g_1(s_{l,c,m} \mathbf{1} + \mathbf{z}_{l,c,m}) + \tilde{\mathbf{e}}_{l,c,m}),$$

where  $\tilde{\mathbf{s}}$  is of dimension  $4 \times 16 \times 13 \times (4 \times 3 \times 2 \times n_f)$ . This is the case, since each EIT signal ( $4 \times 16 \times 13$ ) involves four electrodes and each  $x$ ,  $y$ , and  $z$  coordinate is encoded by sine-cosine-pairs with  $n_f$  different frequencies.

The signal input sequence for RESIST consists of individual measurements in the form of embedding vectors. A natural question is whether individual signals within a measurement cycle should be represented as a measurement or an entire cycle. In the former case, the sequence would consist of  $4 \times 16 \times 13$  input vectors, while in the latter only  $4 \times 16$  input vectors would be used. The latter also gives the model an inductive bias for the coherence of the signals within a cycle. Our experiments show that – for the given data set size – the second option performs better.

**Model Architecture** We follow the transformer architecture proposed by Vaswani et al. (2017) and

process the EIT measurement sequence by self-attention blocks, where each block consists of a multi-head attention layer and a feed forward layer. LayerNorm (Ba et al., 2017) is used before and after the multi-head attention, and skip connections are used before and after the feed forward layer.

After processing the signals and electrode positions, we use 3D points  $\mathbf{p}$  from our volume meshes for the query vector of the cross-attention blocks. These points initially live in real world space and are therefore normalized with the same statistics as the electrode positions. We also apply the identical positional encoding to the points. The self-attended signals are used to form the key and value in the multi-head attention layer within the cross-attention block. Here, we deviate from the transformer architecture and leave out the self-attention between the points as this would lead to a large computational overhead. We found that the positional encoding of the points already introduces a sufficient locality bias to the model.

After the cross-attention blocks, the output features for each point are used in a final feed forward layer to predict the conductivity of the point in the tomogram volume. The final feed forward layer is an MLP with ReLU activation. We train RESIST with a coordinate-based MSE loss and boost the loss of coordinates with lung tissue by a scalar factor. See Appendix A for further implementation details.

## 4. Results

Here we report the results of the RESIST model for a test set including simulations of 30 subjects. The evaluation metrics are the root mean squared error and R-squared across all tomogram pixels (RMSE and  $R^2$ ) and across lung pixels (LRMSE and  $LR^2$ ). The latter will be explained in detail below. RMSE and LRMSE are in S/m and thus describe an approximate absolute deviation from the ground truth conductivity. For visualization purposes we will focus on the first electrode level and refer to Appendix B for more detailed tomograms of the subjects. Please note that our network has a strong spatial prior for upper human body shapes, thus we cannot readily apply it to other domains. In addition, there are no public datasets containing potential differences and electrode positions in 3D as inputs and conductivity values as targets to train and evaluate the model on a different domain.

The RMSE in our test set increases with decreasing lung conductivity from 0.091 for a lung conductivity of 0.2 to 0.100 for 0.05 S/m. The LRMSE lies between 0.014 and 0.019. Across all lung conductivity values the RMSE is 0.096 and the LRMSE 0.017 S/m (Table 1). This shows that RESIST is able to reliably recover the conductivity of lung tissue from the signals and electrode positions with an average relative error between 9.5 and 30% of the true conductivity.

Also visually, the model is able to recover different lung conductivities from the measurements with a comparably low LRMSE (Figure 3). Additionally, the body shape of the test subject is apparent showing only minor deviations, and the LRMSE is comparably low (max 0.012 S/m; Figure 3).

However, the tomogram appears blurred, and some details from the ground truth conductivity distribution cannot be recovered from the signals. This includes, for example, the rib cage and individual blood vessels. In addition, the performance of the RESIST model varies with the topography of the patient. In our test set, we found greater errors arising from greater amounts of subcutaneous fat, an unusual organ location, or no exact supine position. We encourage the interested reader to investigate further cases in Appendix B.1. Nevertheless, the model is also reliable in distinguishing the individual lung conductivity values for these cases, but struggles with the correct body shape and organ position. The main problem here is rather to be found in the prior of the implicit network. This is too heavily biased towards subjects in the supine position with the natural organ topography. A more diverse training set could regularize this bias (Appendix C). On the other hand, this bias is necessary for the model to learn a prior for the anatomical position of tissue and general conductivity distribution of human bodies. Generally, an exact topographical reconstruction cannot be expected due to the low resolution of the signals. Instead, the focus is on the reasonably accurate reconstruction of the conductivity in the lung.

However, the aforementioned inaccuracy leads to a problem in evaluating the tomograms because the morphology of the lungs in the tomograms can differ from the morphology in the volume mesh. As a result, a metric that compares true and predicted conductivity coordinate by coordinate may have high errors, although the overall conductivity prediction of lung tissue is not far off. Therefore, we shrink the lung mask using linear erosion and compute the LRMSE on the eroded masks instead. The red contour visible

Table 1: RMSE, LRMSE,  $R^2$  and  $LR^2$  for electrode level tomograms of SIRT and RESIST on all lung conductivity values, and broken down by the respective lung conductivity. Standard deviation in italic. Note, that the RMSE is not meaningful for SIRT.

	<b>RMSE</b>	<b>LRMSE</b>	<b><math>R^2</math></b>	<b><math>LR^2</math></b>
<b>SIRT</b>	-	0.321	-	-35.344
<b>RESIST</b>	$0.096 \pm 0.001$	$0.017 \pm 0.002$	$0.645 \pm 0.011$	$0.912 \pm 0.018$
0.2 S/m	$0.091 \pm 0.002$	$0.019 \pm 0.007$	$0.691 \pm 0.011$	-
0.1 S/m	$0.095 \pm 0.002$	$0.018 \pm 0.002$	$0.647 \pm 0.013$	-
0.07 S/m	$0.098 \pm 0.001$	$0.014 \pm 0.001$	$0.626 \pm 0.011$	-
0.05 S/m	$0.100 \pm 0.001$	$0.015 \pm 0.0001$	$0.611 \pm 0.009$	-

in Figure 3 shows those eroded lung masks and the corresponding LRMSE in the red box.

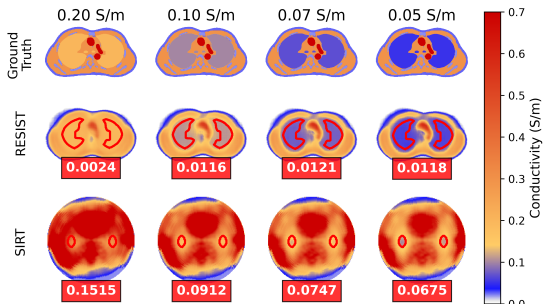


Figure 3: Tomograms of RESIST and SIRT. The red box shows the LRMSE for coordinates in the eroded lung mask (red contour). The lung mask for SIRT was added manually.

Despite using only four different values for the lung conductivity, RESIST does not overfit but rather learns the interpolation between individual values (Appendix B.4). To illustrate this generalization property, we trained RESIST by omitting the data once for 0.1 and once for 0.07 S/m. Evaluating the LRSME on the left out conductivity results in an average increase of 0.019 (LRMSE 0.037) and 0.006 (0.020) S/m, demonstrating that RESIST is able to predict conductivity values on which it was not trained.

Comparing RESIST with the 3D methods mentioned in Section 2 is difficult, since they cannot be readily applied to the simulated signals in order to reconstruct the conductivity distribution of complex

3D shapes. Therefore, we compare RESIST with the 2.5D SIRT algorithm (Just et al., 2007). Although SIRT is able to differentiate between the conductivity values of the lungs to a certain extent, the tomograms are difficult to interpret on their own and do not resemble the true conductivity distribution (Figure 3). In comparison, RESIST comes closer to the ground truth conductivity distribution and resembles the true body shape and tissue location, e.g. for heart and lungs. SIRT is also quantitatively significantly worse with an almost 20-fold higher LRMSE (Table 1).

#### 4.1. Noise Robustness

EIT measurements are subject to interference, resulting in real measurements being distorted by noise. Common sources of interference are the EIT device itself or crosstalk of signals between cables. Qu et al. (2021) approximately quantified the noise level for common EIT devices at  $SNR \geq 60$  dB. Additionally, Hahn et al. (2010) found that signals originating from electrode pairs that are adjacent to the feeding electrodes are less affected by noise than those that are more distant. Within a cycle, the SNR decreases until the recording electrodes furthest away from the feeding electrodes are reached and then increases again. This relationship can be approximated conservatively by a cosine function with an amplitude of 30 (60 – 30) dB and an intercept of 30 dB (Figure 17). We mimic this behaviour by adding Gaussian noise according to the expected SNR for each signal within a cycle. This is done by z-scoring each of the  $4 \times 16 \times 13$  signals. This way we can assume that every signal follows a standard normal distribution with a mean of 0 and a variance of 1. The SNR is de-

Table 2: Test results with standard deviation for four signal noise intensities ( $SNR_{high}/SNR_{low}$ ) using four noise seeds.

SNR	60/30dB	30/0dB	0/-10dB	-10/-20dB
<b>RMSE</b>	$0.096 \pm 0.001$	$0.097 \pm 0.001$	$0.107 \pm 0.001$	$0.176 \pm 0.007$
<b>LRMSE</b>	$0.017 \pm 0.002$	$0.020 \pm 0.002$	$0.042 \pm 0.004$	$0.092 \pm 0.012$
<b>R<sup>2</sup></b>	$0.645 \pm 0.011$	$0.640 \pm 0.009$	$0.562 \pm 0.008$	$-0.192 \pm 0.097$
<b>LR<sup>2</sup></b>	$0.912 \pm 0.018$	$0.877 \pm 0.025$	$0.463 \pm 0.105$	$-1.522 \pm 0.680$

fined as:  $SNR_{dB} = 20 \cdot \log_{10} \frac{U_{signal}}{U_{noise}}$ , where  $U$  refers to the voltage of the signal or noise channel. We can use the root mean square (RMS) of the signal for  $U_{signal}$ , which is equal to its standard deviation. Plugging in the desired SNR for our signal within the cycle, we can solve for the noise variance that has to be added.

Even at comparatively high noise levels of up to  $SNR_{high} = 30$  dB and  $SNR_{low} = 0$  dB, the model generates tomograms with a low error (Table 2). The appearance only deteriorates dramatically at -10 and -20 dB (Figure 4). This is also evident from the high standard deviation within the lung contour.

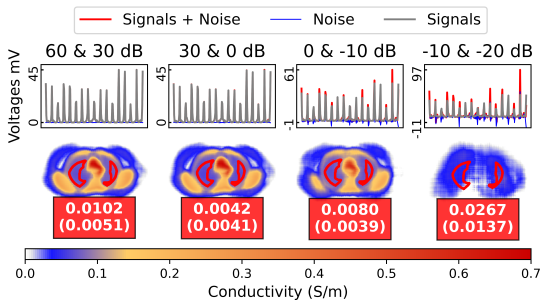


Figure 4: Clean signals, corrupted signals, absolute noise added (top) and corresponding tomograms (bottom). Red box shows LRMSE and standard deviation of eroded lungs.

In summary, the model demonstrates sufficient noise robustness, particularly when considering that the left tomogram in Figure 4 corresponds to the expected noise level of real EIT measurements.

#### 4.2. Sensitivity to Electrode Positions

Recording the exact electrode positions on the body is an additional difficulty with real EIT measurements,

especially for immobile patients for whom a 3D scan of the body with electrodes attached is difficult. Even with mobile patients, the electrode positions shift when they stand up or change their posture, for example by raising their arms. We therefore shift the electrode position using Gaussian noise to investigate the robustness of the model with respect to inaccuracies in electrode positions.

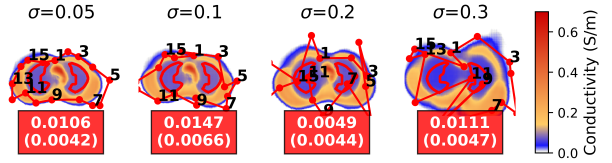


Figure 5: Electrodes shifted by four different noise levels in 2D. Red box shows LRMSE and standard deviation of eroded lungs.

We randomly move the electrodes around in the 3D output space using Gaussian noise with a standard deviation  $\sigma$  of 0.05, 0.1, 0.2 and 0.3. A noise level of  $\sigma = 0.3$  leads to a significant distortion of the electrode positions as can be observed in Figure 5. Nonetheless, the LRMSE remains low, and the standard deviation of the lung coordinates increases only minimally. The RMSE for the whole test set increases by 0.009 S/m for  $\sigma = 0.3$  (3), which is illustrated by the drastic effect on the body shape in Figure 5. However, the general topography within the body remains reasonable. RESIST seems to use the electrode positions only for an approximate body shape estimation, while the EIT signals have a much stronger influence on the conductivity distribution within this body shape, as shown in Section 4.1.

Table 3: Test results and standard deviation for four different electrode position noise intensities using four noise seeds.

Noise Level	$\sigma = 0.05$	$\sigma = 0.10$	$\sigma = 0.20$	$\sigma = 0.30$
<b>RMSE</b>	$0.096 \pm 0.001$	$0.097 \pm 0.001$	$0.101 \pm 0.001$	$0.105 \pm 0.001$
<b>LRMSE</b>	$0.017 \pm 0.002$	$0.018 \pm 0.002$	$0.021 \pm 0.002$	$0.025 \pm 0.002$
<b>R<sup>2</sup></b>	$0.643 \pm 0.011$	$0.636 \pm 0.011$	$0.610 \pm 0.011$	$0.575 \pm 0.011$
<b>LR<sup>2</sup></b>	$0.911 \pm 0.018$	$0.904 \pm 0.020$	$0.872 \pm 0.028$	$0.812 \pm 0.034$

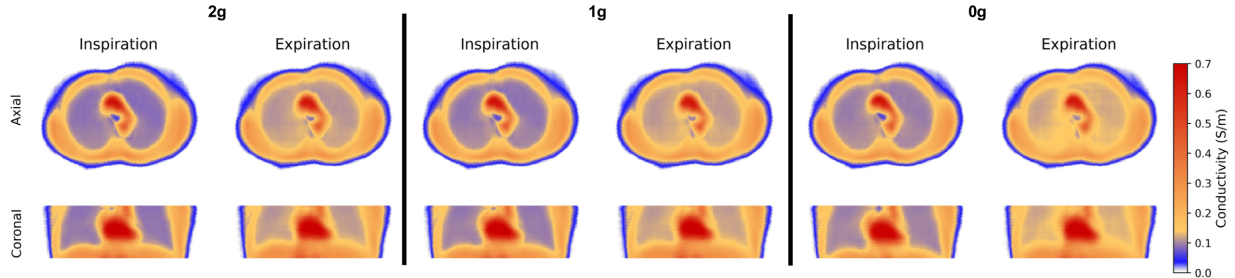


Figure 6: Tomograms from axial and coronal view for real measurements recorded in 2g, 1g and zero gravity.

#### 4.3. Application on Real Measurements

To compare our results on simulation data with real measurements, we use EIT measurements that were taken during a parabolic flight with 2g, 1g and without gravitational force. In zero gravity, the distribution of conductivity in the lungs can be assumed to be approximately homogeneous, thereby conforming to the simplifying assumption of the simulations (Hahn et al., 2013). Figure 6 shows the tomograms in axial and coronal view during expiration and inspiration. For all three gravitational forces, the lung expansion in the direction of the abdominal cavity during inhalation is clearly identifiable. The lungs also have a higher conductivity value on exhalation, as expected due to the smaller surface area of the aveoli and the low volume of gas in the lungs. This can be observed for 2g, 1g and 0g, with the effect being most pronounced for the latter. This demonstrates that RESIST is also capable of generating topographically correct and easily interpretable tomograms for real measurements.

#### 5. Conclusion

In this paper we have introduced RESIST, an implicit spatially-aware transformer model that enables the direct mapping of sparse signals to a continuous output space in 3D. In the context of EIT, the strong prior of the implicit network on human bodies and an extensive data set of realistic simulations allowed us to generate interpretable tomograms for simulated and real measurements. The model is robust to signal noise and variations in electrode positions. We are confident that the model has potential that can be further exploited by additional and more diverse simulations in the future.

## Acknowledgments

This research was funded by the German Aerospace Center (*DLR; FKZ 50WK2274B*). The authors gratefully acknowledge the computing time granted by the Resource Allocation Board and provided on the supercomputer Emmy/Grete at NHR@Göttingen as part of the NHR infrastructure. The calculations for this research were conducted with computing resources under the project *nix00012*. We further acknowledge the authors of TotalSegmentator for providing the pretrained model used for segmentation in this work, and the Cancer Imaging Archive (TCIA) for supplying the data necessary for the study.

## References

- Andy Adler and Robert Guardo. A neural network image reconstruction technique for electrical impedance tomography. *IEEE Transactions on Medical Imaging*, 13(4):594–600, 1994.
- Andy Adler, John H Arnold, Richard Bayford, Andrea Borsic, Brian Brown, Paul Dixon, Theo JC Faes, Inéz Frerichs, Hervé Gagnon, Yvo Gärber, et al. Greit: a unified approach to 2d linear eit reconstruction of lung images. *Physiological measurement*, 30(6):S35, 2009.
- Melody Alsaker and Jennifer L Mueller. A d-bar algorithm with a priori information for 2-dimensional electrical impedance tomography. *SIAM Journal on Imaging Sciences*, 9(4):1619–1654, 2016.
- Melody Alsaker and Jennifer L Mueller. Use of an optimized spatial prior in d-bar reconstructions of eit tank data. *Inverse Problems and Imaging*, 12(4):883–901, 2018.
- Melody Alsaker, Sarah Jane Hamilton, and Andreas Hauptmann. A direct d-bar method for partial boundary data electrical impedance tomography with a priori information. *Inverse Problems and Imaging*, 11(3):427–454, 2017.
- Jimmy Ba, Jamie Ryan Kiros, and Geoffrey E. Hinton. Layer normalization. In *Proceedings of the 34th International Conference on Machine Learning (ICML)*, 2017. URL <https://arxiv.org/abs/1607.06450>.
- Jiezhang Cao, Qin Wang, Yongqin Xian, Yawei Li, Bingbing Ni, Zhiming Pi, Kai Zhang, Yulun Zhang, Radu Timofte, and Luc Van Gool. Ciaosr: Continuous implicit attention-in-attention network for arbitrary-scale image super-resolution, 2023. URL <https://arxiv.org/abs/2212.04362>.
- Yinbo Chen and Xiaolong Wang. Transformers as meta-learners for implicit neural representations, 2022. URL <https://arxiv.org/abs/2208.02801>.
- Zhou Chen, Yunjie Yang, Jiabin Jia, and Pierre Bagnaninchi. Deep learning based cell imaging with electrical impedance tomography. In *2020 IEEE International Instrumentation and Measurement Technology Conference (I2MTC)*, pages 1–6, 2020. doi: 10.1109/I2MTC43012.2020.9128764.
- Alexey Dosovitskiy, Lucas Beyer, Alexander Kolesnikov, Dirk Weissenborn, Xiaohua Zhai, Thomas Unterthiner, Mostafa Dehghani, Matthias Minderer, Georg Heigold, Sylvain Gelly, et al. An image is worth 16x16 words: Transformers for image recognition at scale. *arXiv preprint arXiv:2010.11929*, 2020.
- Yuwei Fan and Lexing Ying. Solving electrical impedance tomography with deep learning. *Journal of Computational Physics*, 404:109119, 2020. ISSN 0021-9991. doi: <https://doi.org/10.1016/j.jcp.2019.109119>. URL <https://www.sciencedirect.com/science/article/pii/S0021999119308241>.
- Inéz Frerichs, Marcelo Amato, Anton Kaam, David Tingay, Zhanqi Zhao, Bartłomiej Grychtol, Marc Bodenstein, Hervé Gagnon, Stephan Bohm, Eckhard Teschner, Ola Stenqvist, Tommaso Mauri, Vinicius Torsani, Luigi Camporota, Andreas Schibler, Gerhard Wolf, Diederik Gommers, Steffen Leonhardt, and Andy Adler. Chest electrical impedance tomography examination, data analysis, terminology, clinical use and recommendations: consensus statement of the translational eit development study group. *Thorax*, 72:83–93, 01 2017. doi: 10.1136/thoraxjnl-2016-208357.
- Camelia Gabriel and Sami Gabriel. Compilation of the dielectric properties of body tissues at rf and microwave frequencies, 1996.
- Camelia Gabriel, Sami Gabriel, and E Corthout. The dielectric properties of biological tissues: I. literature survey. *Physics in Medicine and Biology*, 41(11):2231, nov 1996. doi: 10.1088/0031-9155/

- 41/11/001. URL <https://dx.doi.org/10.1088/0031-9155/41/11/001>.
- Deepti Garg and Vikas Goel. Design and development of electrical impedance tomography (eit) based system. *International Journal of Computer Applications*, 74(7), 2013.
- S. Gatidis and T. Kuestner. A whole-body fdg-pet/ct dataset with manually annotated tumor lesions (fdg-pet-ct-lesions). Dataset, 2022. The Cancer Imaging Archive.
- Günter Hahn, Anita Just, Taras Dudykevych, Inéz Frerichs, Jose Hinz, Michael Quintel, and Gerhard Hellige. Imaging pathologic pulmonary air and fluid accumulation by functional and absolute eit. *Physiological Measurement*, 27(5):S187, apr 2006. doi: 10.1088/0967-3334/27/5/S16. URL <https://dx.doi.org/10.1088/0967-3334/27/5/S16>.
- Günter Hahn, Jörg Dittmar, Anita Just, Michael Quintel, and Gerhard Hellige. Different approaches for quantifying ventilation distribution and lung tissue properties by functional eit. *Physiological Measurement*, 31(8):S73, jul 2010. doi: 10.1088/0967-3334/31/8/S06. URL <https://dx.doi.org/10.1088/0967-3334/31/8/S06>.
- Günter Hahn, Anita Just, Gerhard Hellige, Jörg Dittmar, and Michael Quintel. How absolute eit reflects the dependence of unilateral lung aeration on hyper-gravity and weightlessness? *Physiological Measurement*, 34(9):1063, aug 2013. doi: 10.1088/0967-3334/34/9/1063. URL <https://dx.doi.org/10.1088/0967-3334/34/9/1063>.
- Sarah Hamilton, David Isaacson, Ville Kolehmainen, Peter Muller, Jussi Toivanen, and Patrick Bray. 3d eit reconstructions from electrode data using direct inversion d-bar and calderon methods. 07 2020. doi: 10.48550/arXiv.2007.03018.
- Sarah J Hamilton, Jennifer L Mueller, and Melody Alsaker. Incorporating a spatial prior into non-linear d-bar eit imaging for complex admittivities. *IEEE transactions on medical imaging*, 36(2):457–466, 2016.
- Sarah Jane Hamilton and Andreas Hauptmann. Deep d-bar: Real-time electrical impedance tomography imaging with deep neural networks. *IEEE transactions on medical imaging*, 37(10):2367–2377, 2018.
- Jonathan Ho, Ajay Jain, and Pieter Abbeel. Denoising diffusion probabilistic models, 2020. URL <https://arxiv.org/abs/2006.11239>.
- Fabian Isensee, Jens Petersen, Andre Klein, David Zimmerer, Paul F. Jaeger, Simon Kohl, Jakob Wasserthal, Gregor Koehler, Tobias Norajitra, Sebastian Wirkert, and Klaus H. Maier-Hein. nnunet: Self-adapting framework for u-net-based medical image segmentation, 2018. URL <https://arxiv.org/abs/1809.10486>.
- John Jumper, Richard Evans, Alexander Pritzel, Tim Green, Michael Figurnov, Olaf Ronneberger, Kathryn Tunyasuvunakool, Russ Bates, Augustin Žídek, Anna Potapenko, et al. Highly accurate protein structure prediction with alphafold. *nature*, 596(7873):583–589, 2021.
- Anita Just, T Küpper, and F Jacobs. Core imaging by electrical resistivity tomography. *Proc. 4th SEGJ Int Symp*, pages 231–237, 1998.
- Anita Just, Carsten Ruecker, Günter Hahn, and Gerhard Hellige. Sensitivity of two different reconstruction algorithms to body shape and electrode position errors in absolute eit. In *13th International Conference on Electrical Bioimpedance and the 8th Conference on Electrical Impedance Tomography: ICEBI 2007, August 29th-September 2nd 2007, Graz, Austria*, pages 404–407. Springer, 2007.
- Diederik P Kingma and Max Welling. Auto-encoding variational bayes, 2022. URL <https://arxiv.org/abs/1312.6114>.
- Kim Knudsen, Matti Lassas, Jennifer L Mueller, and Samuli Siltanen. D-bar method for electrical impedance tomography with discontinuous conductivities. *SIAM Journal on Applied Mathematics*, 67(3):893–913, 2007.
- Xiuyan Li, Yong Zhou, Jianming Wang, Qi Wang, Yang Lu, Xiaojie Duan, Yukuan Sun, Jingwan Zhang, and Zongyu Liu. A novel deep neural network method for electrical impedance tomography. *Transactions of the Institute of Measurement and Control*, 41(14):4035–4049, 2019.
- Shengheng Liu, Jiabin Jia, Yimin D. Zhang, and Yunjie Yang. Image reconstruction in electrical impedance tomography based on structure-aware sparse bayesian learning. *IEEE Transactions on*

- Medical Imaging*, 37(9):2090–2102, 2018. doi: 10.1109/TMI.2018.2816739.
- Lars Mescheder, Michael Oechsle, Michael Niemeyer, Sebastian Nowozin, and Andreas Geiger. Occupancy networks: Learning 3d reconstruction in function space. In *Proceedings of the IEEE/CVF conference on computer vision and pattern recognition*, pages 4460–4470, 2019.
- Ben Mildenhall, Pratul P Srinivasan, Matthew Tancik, Jonathan T Barron, Ravi Ramamoorthi, and Ren Ng. Nerf: Representing scenes as neural radiance fields for view synthesis. *Communications of the ACM*, 65(1):99–106, 2021.
- Jennifer L Mueller and Samuli Siltanen. Direct reconstructions of conductivities from boundary measurements. *SIAM Journal on Scientific Computing*, 24(4):1232–1266, 2003.
- COMSOL Multiphysics. Introduction to comsol multiphysics®. *COMSOL Multiphysics, Burlington, MA, accessed Feb, 9:2018*, 1998.
- Songyou Peng, Michael Niemeyer, Lars Mescheder, Marc Pollefeys, and Andreas Geiger. Convolutional occupancy networks. In *Computer Vision–ECCV 2020: 16th European Conference, Glasgow, UK, August 23–28, 2020, Proceedings, Part III 16*, pages 523–540. Springer, 2020.
- Shiyang Qu, Ming Dai, Shaolong Wu, et al. System introduction and evaluation of the first chinese chest eit device for icu applications. *Scientific Reports*, 11(1):19273, 2021. doi: 10.1038/s41598-021-98793-0. URL <https://doi.org/10.1038/s41598-021-98793-0>.
- Alec Radford, Karthik Narasimhan, Tim Salimans, and Ilya Sutskever. Improving language understanding by generative pre-training. Technical report, OpenAI, 2018. URL [https://cdn.openai.com/research-covers/language-unsupervised/language\\_understanding\\_paper.pdf](https://cdn.openai.com/research-covers/language-unsupervised/language_understanding_paper.pdf).
- Samuli Siltanen, Jennifer Mueller, and David Isaacson. An implementation of the reconstruction algorithm of a nachman for the 2d inverse conductivity problem. *Inverse Problems*, 16(3):681, 2000.
- Vincent Sitzmann, Julien Martel, Alexander Bergman, David Lindell, and Gordon Wetzstein. Implicit neural representations with periodic activation functions. *Advances in neural information processing systems*, 33:7462–7473, 2020.
- Yang Song, Jascha Sohl-Dickstein, Diederik P. Kingma, Abhishek Kumar, Stefano Ermon, and Ben Poole. Score-based generative modeling through stochastic differential equations, 2021. URL <https://arxiv.org/abs/2011.13456>.
- Synopsys, Inc. Synopsys simpleware software. <https://www.synopsys.com/simpleware.html>, 2020.
- Ashish Vaswani, Noam Shazeer, Niki Parmar, Jakob Uszkoreit, Llion Jones, Aidan N Gomez, Łukasz Kaiser, and Illia Polosukhin. Attention is all you need. *Advances in neural information processing systems*, 30, 2017.
- Peng Wang, Lili Xie, and Yicai Sun. Application of pso algorithm and rbf neural network in electrical impedance tomography. In *2009 9th International Conference on Electronic Measurement & Instruments*, pages 2–517. IEEE, 2009.
- Jakob Wasserthal, Hanns-Christian Breit, Manfred T Meyer, Maurice Pradella, Daniel Hinck, Alexander W Sauter, Tobias Heye, Daniel T Boll, Joshy Cyriac, Shan Yang, et al. Totalsegmentator: robust segmentation of 104 anatomic structures in ct images. *Radiology: Artificial Intelligence*, 5(5), 2023.
- Yang Wu, Bai Chen, Kai Liu, Chengjun Zhu, Huaping Pan, Jiabin Jia, Hongtao Wu, and Jiafeng Yao. Shape reconstruction with multiphase conductivity for electrical impedance tomography using improved convolutional neural network method. *IEEE sensors journal*, 21(7):9277–9287, 2021.
- Yunjie Yang, Jiabin Jia, Stewart Smith, Nadira Jamil, Wesam Gamal, and Pierre-Olivier Bagnanichi. A miniature electrical impedance tomography sensor and 3-d image reconstruction for cell imaging. *IEEE Sensors Journal*, 17(2):514–523, 2017. doi: 10.1109/JSEN.2016.2631263.
- Ming Ye, Tong Zhou, Xiaocheng Li, Lu Yang, Kai Liu, and Jiafeng Yao. U<sup>2</sup>-net for 3d electrical impedance tomography with combined electrodes. *IEEE Sensors Journal*, 23(5):4327–4335, 2023. doi: 10.1109/JSEN.2022.3178119.

Jaeik Yoo, Chaejeong Seo, Jong Chul Park, and Sungdo Woo. Point-cloud transformer for 3-d electrical impedance tomography. In *Proceedings of the IEEE/CVF Conference on Computer Vision and Pattern Recognition (CVPR)*, pages 13643–13652, 2023.

Alex Yu, Vickie Ye, Matthew Tancik, and Angjoo Kanazawa. pixelnerf: Neural radiance fields from one or few images. In *Proceedings of the IEEE/CVF conference on computer vision and pattern recognition*, pages 4578–4587, 2021.

Ellen D. Zhong, Tristan Bepler, Joseph H. Davis, and Bonnie Berger. Reconstructing continuous distributions of 3d protein structure from cryo-em images, 2020. URL <https://arxiv.org/abs/1909.05215>.

## Appendix A. Implementation Details

We train RESIST with a coordinate-based MSE loss and boost the loss of coordinates with lung tissue by a scalar factor. This leads to a greater contribution of deviations of the predicted conductivity in the lung area and thus sets the focus in training on the reconstruction of the lung area.

$$L_{LMSE} = \frac{1}{N} \sum_{n=1}^N \sum_{i \sim U} b_{i,n} \cdot (f(\mathbf{s}_n, \mathbf{e}_n, \mathbf{p}_i) - r_{i,n})^2$$

where  $N$  is the number of test simulations and  $U$  is a uniform distribution over the indices of the discrete grid of the ground true conductivities.  $b_{n,i}$  is a boost factor that assigns a higher loss for coordinates that lie in the lung:

$$b_{n,i} = \begin{cases} \beta & \text{if } p_i \in V_n^{lung} \\ 1 & \text{else} \end{cases}$$

A boost factor of  $\beta = 8$  has proven to be reasonable. We use 5 decoder and encoder blocks with 256 nodes each for the multi-head attention blocks and map these up to 1024 nodes in the feed-forward blocks with GeLU activation. The final feed-forward block, on the other hand, uses only 256 nodes and a ReLU activation to ensure positive conductivity values. We also use a dropout of 0.2 in the multi-head attention and feed-forward blocks except for the last one. We use a  $n_f = 10$  for the positional encoding of electrodes and coordinates and a signal embedding  $z_{lcm}$  of dimension 8. During training, we exclude each measurement cycle with a probability of  $\pi = 0.1$ . Furthermore, we use random rotation and random translation of the true conductivity distribution in the output space as data augmentations. Adam with a learning rate of 0.0001 is used. We train the model for a total of 100 epochs with batch size 4 and randomly sample 100,000 coordinates for each training subject in each epoch. For inference, we use the checkpoint that has the lowest RMSE lung loss (see Section 4). We found that the model easily overfits on the four discrete values for lung conductivity. We believe that the extension of the data set to more diverse lung conductivity values would decrease the problem of overfitting and result in sharper tomograms.

## Appendix B. Results

Further tomograms of test subjects can be found below. The figures show the descending body level on the y-axis and a descending lung conductivity along the x-axis.

### B.1. Further Example Tomograms

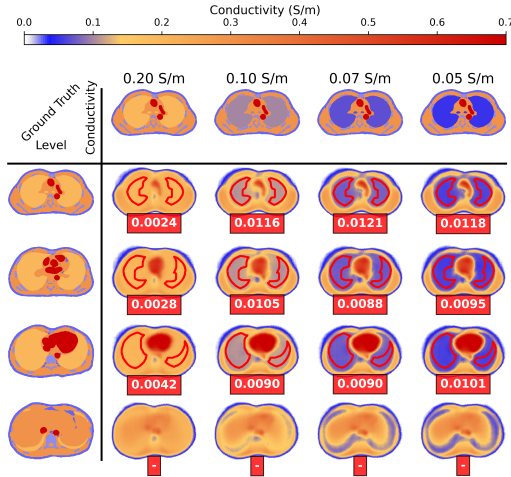


Figure 7: Test Subject 1

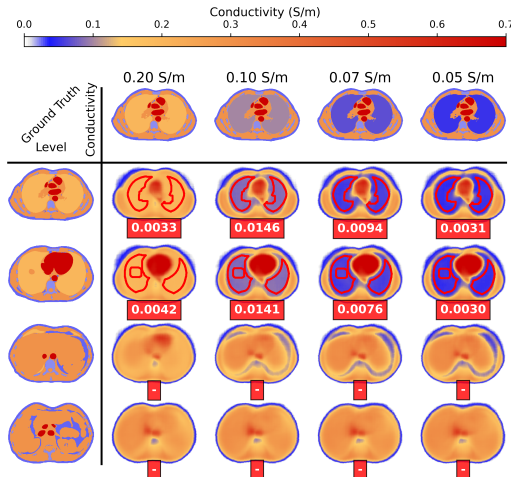


Figure 8: Test Subject 2

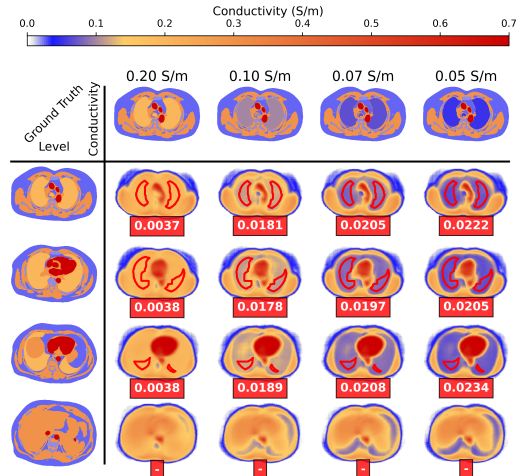


Figure 9: Test Subject 3

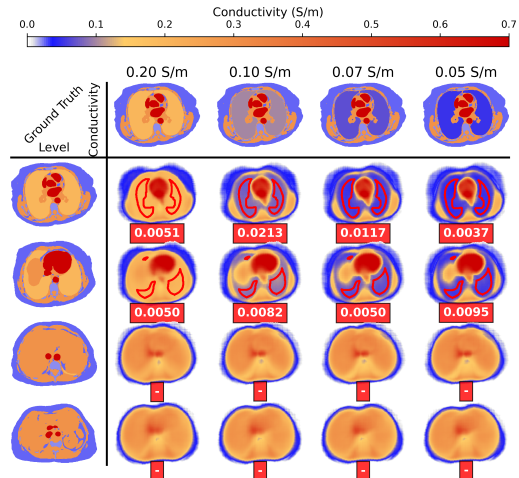


Figure 10: Test Subject 4

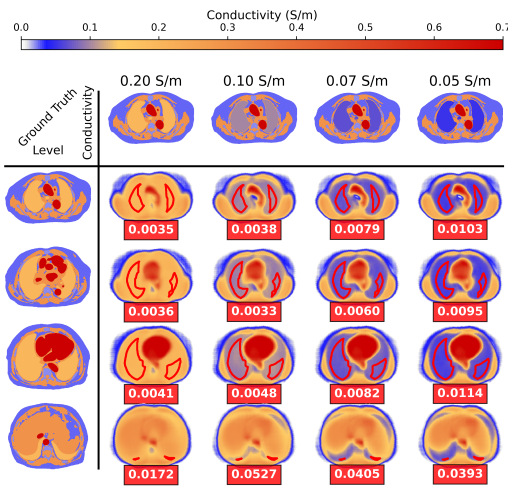


Figure 11: Test Subject 5

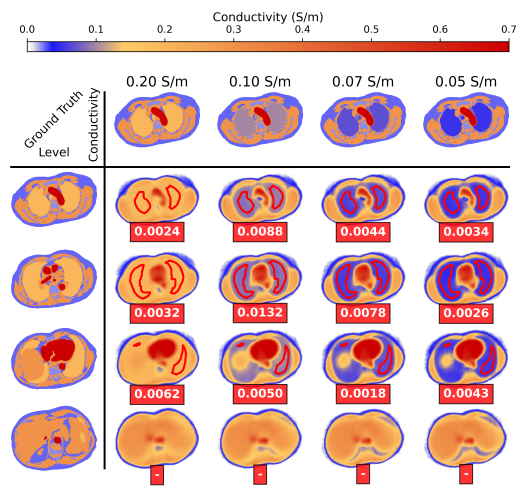


Figure 13: Test Subject 7

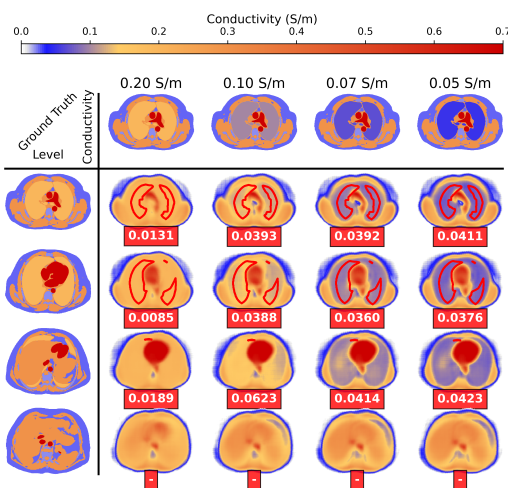


Figure 12: Test Subject 6

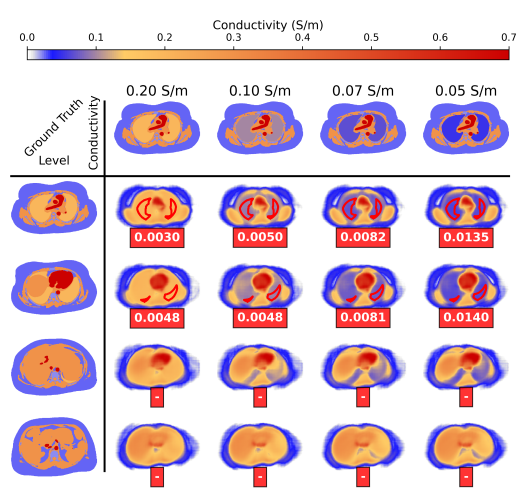


Figure 14: Test Subject 8

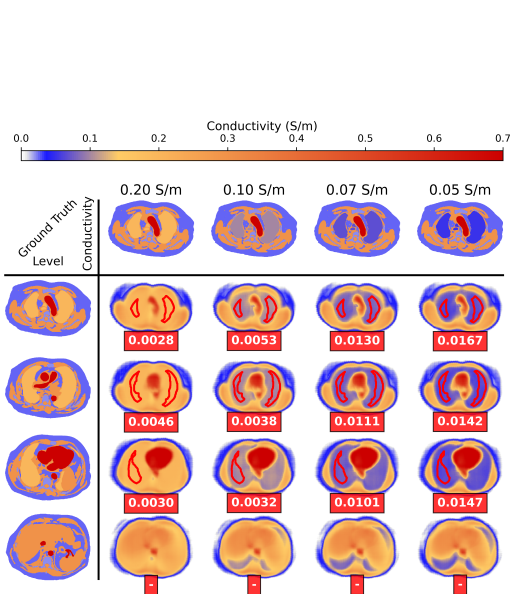


Figure 15: Test Subject 9

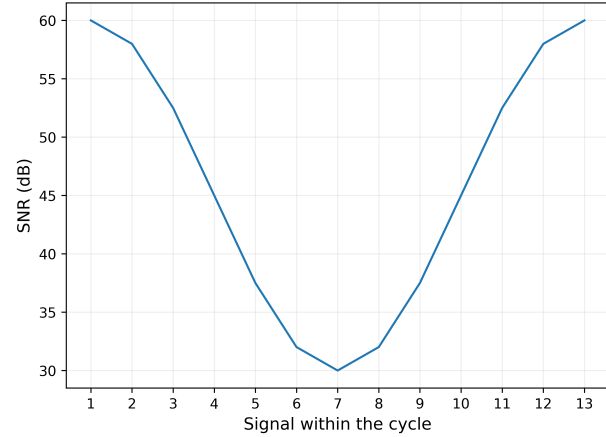
**B.2. Noise Robustness**

Figure 17: Desired SNR for signals within a cycle to mimic real EIT measurements. Electrodes furthest away from the feeding electrodes will have a higher noise level than those that are close by.

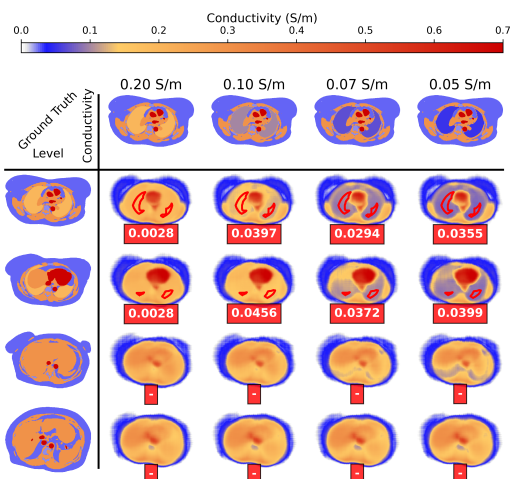


Figure 16: Test Subject 10

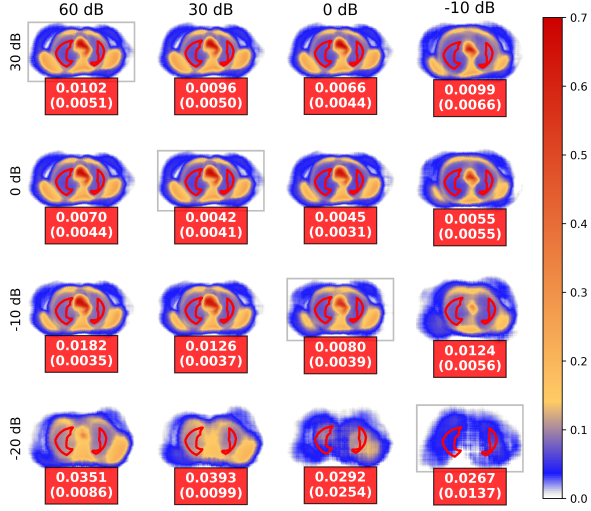


Figure 18: Tomograms with noised signals.  $SNR_{high}$  is varied along the columns,  $SNR_{low}$  along the rows.

### B.3. Implicit 3D Properties

One of the advantages of our model is that it is a continuous function in 3D, thus any 3D coordinate can be queried individually, allowing to create tomograms for any position and angle along the body. This property is shown in Figure 19 for an axial, sagittal and coronal section of the tomogram space. We queried 512 equidistant slices along the z dimension for the test patient and obtain a comparably smooth gradient along the z dimension, although the model was trained with points from only 15 different levels along the z dimension for each subject.

### B.4. Interpolation Properties

Ohm’s law states that voltage and resistance are in a linear relationship. To test whether RESIST learned this property, we can translate the lung conductivity to resistivity and linearly interpolate between the signals obtained from different resistivity values used for the lung during simulation. We would expect a smooth transition between conductivity values in the resulting tomograms. Figure 20 shows the results of linear interpolation and confirms that our model learned a smooth transition. However, it is also clearly visible, that the predictions between the

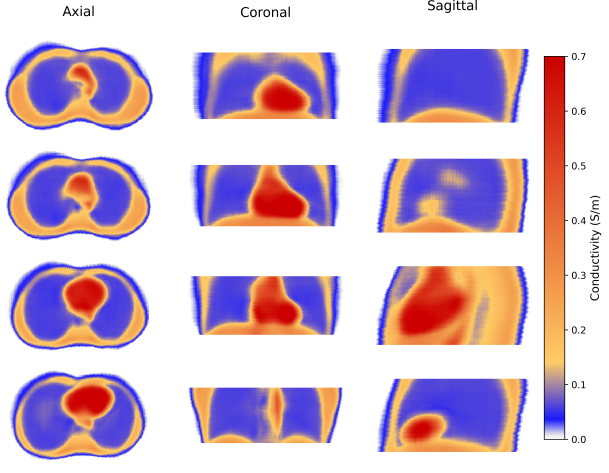


Figure 19: Tomograms of a test patient for axial, coronal and sagittal anatomical views.

conductivity values of 0.2 and 0.1 S/m (top row in Figure 20) are less accurate than the bottom row. This shows that a greater variation and smaller gaps between conductivity values used for the simulations has the potential to enable a better generalization of the model.

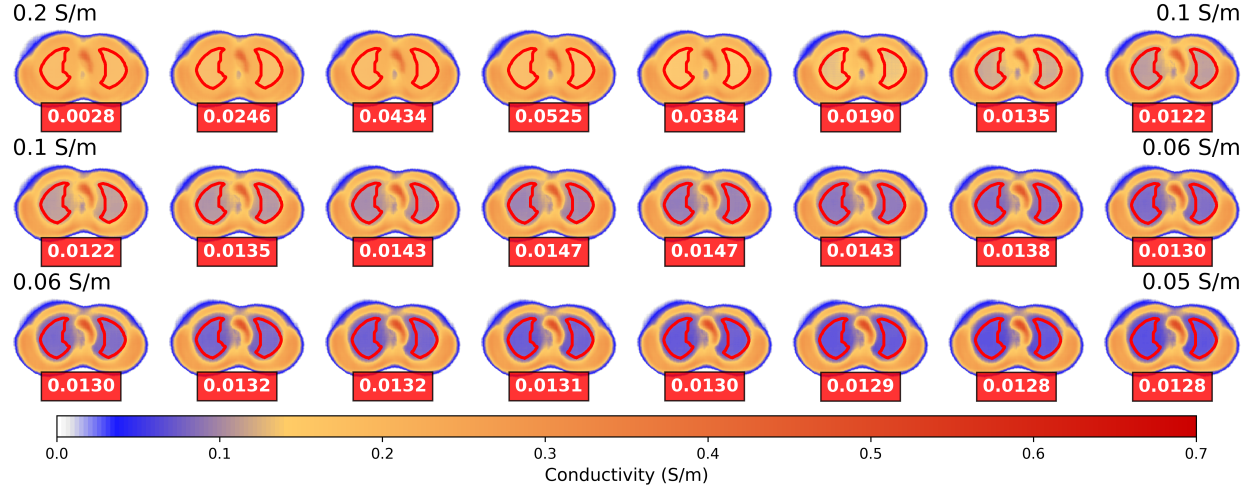


Figure 20: Interpolation of the signals generated by successive conductivity values for the lung.

### Appendix C. Limitations

Our approach involves several simplifications. We grouped finely segmented CT classes into just five categories, assuming uniform conductivity within each group, including homogeneous lung tissue. Additionally, our simulations altered only lung conductivity, not shape, despite the changes in lung size during breathing. All CTs were taken in the supine position, affecting organ topography and conductivity distribution.

The use of discrete conductivity values and only 16 electrodes per level is another limitation. A broader range of realistic conductivity values for the lung and more electrode positions could improve model generalization. Furthermore, we used the Adjacent Drive method, which excludes potential differences from electrodes at different levels, potentially missing valuable information, particularly in regions between measurement levels. Also, the feeding electrodes were always adjacent, though other arrangements might hold additional insights.